Multi-scale structural investigation of uranium-plutonium mixed oxides $(U_{1-y}Pu_y)O_{2-x}$ with high plutonium content

M-M. Desagulier, J. Martinez, P.M. Martin, F. Lebreton, C. Guéneau, Nicolas Clavier

Multi-scale structural investigation of uranium-plutonium mixed oxides ($U_{1-y}Pu_y)O_{2-x}$ with high plutonium content.

M-M. Desagulier[1], J. Martinez[2], P.M. Martin[1], F. Lebreton[1], C. Guéneau[3], N. Clavier[4].
1 *CEA, DES, ISEC, DMRC, SASP, Univ Montpellier, Marcoule, France*
2 *CEA, DES, ISEC, DMRC, SPTC, Univ Montpellier, Marcoule, France*
3 *Université Paris-Saclay, CEA, SCCME, Gif-sur-Yvette, France*
4 ICSM, *Univ Montpellier, CEA, CNRS, ENSCM, Marcoule, France*

Abstract

Uranium-Plutonium mixed oxides $U_{1-y}Pu_yO_{2-x}$ are considered as the reference fuels for Sodium-cooled Fast neutron Reactors (SFRs). Nevertheless, there is a lack of experimental data on their thermal properties for a Pu content above 0.45. The first step to fill this gap is to manufacture samples with high plutonium contents, which is the purpose of this work. Here, the manufacturing of $U_{1-y}Pu_yO_2$ samples with y = 0.60, 0.65 and 0.70 by a co-milling powder metallurgy process is detailed. Relying on an optimization of each manufacturing step (blending, co-milling, sieving, pelletizing and sintering), in order to obtain dense, monophasic, stoichiometric and homogenous materials.
A multi-scale characterization strategy was used to determine sample microstructural properties including density measurements, Thermal-Ionization Mass Spectrometer (TIMS), ceramography, Electron Probe Micro Analyses, µ-Raman Spectroscopy and X-Ray Diffraction. The results obtained show that dense (> 95% TD), homogenous (chemical distribution of cations and oxygen), monophasic and stoichiometric (O/M = 2.00) samples have been achieved. These properties correspond to those needed to optimize the thermo-physical properties measurements. This also shows that the coupling of multi-scale characterizations is mandatory to evaluate the structural and microstructural properties of this kind of material.

1. Introduction

Currently, in France, the nuclear power plants are pressurized water reactors (PWRs). These reactors are mainly loaded with uranium dioxide (UO_2), with an average enrichment of 3.5% to 5% in the isotope 235 (natural uranium contains only 0.72% of this isotope). For over 50 years, most of the nuclear countries (Europe, USA, Japan, …) have been experimenting with plutonium recycling, leading to the development of mixed oxides (MOX, $(U,Pu)O_2$), for fast and thermal neutron reactors. In the case of PWR, these fuels are have an average plutonium content under 0.12 Pu/(U+Pu) and an oxygen stoichiometry (Oxygen/Metal ratio) of 2.00 [TRE06]. In order to progress towards a closed fuel cycle including reprocessing of spent fuel and extended refueling with MOX fuel, Sodium-cooled Fast neutron Reactors (SFRs) are among the most promising solutions.
In the case of fast neutron reactor fuels, plutonium fraction and Oxygen/Metal ratio (O/M with M = U + Pu) must range between 0.20 to 0.35 and $1.94 \leq O/M < 2.00$, respectively. During irradiation in SFR, a ~1300K thermal gradient along the fuel pellet radius, typically ~ 4 mm, takes place leading to the redistribution of plutonium and oxygen [PEL20]. Actually, the pellet center is enriched in plutonium with a local Pu content of 0.3 for an initial content of 0.2, and depleted in oxygen, as described by Guerin [PEL20]. A higher Pu content of 0.53 is thus expected at the center of the pellet for an initial content of 0.35.Conversely, in the rim region, a depletion in plutonium and a O/M ratio close to 2.00 are observed. These mass transport phenomena along the pellet radius leads to significant local heterogeneities in the thermo-physical properties of the fuel. Moreover, during irradiation, one of the safety margin requirements of the reactor is that the fuel must not reach the melting temperature, even very locally. However, a decrease of the melting temperature is observed when the local plutonium content increases up to 0.5 Pu/(U+Pu) [FOU23, GUEN12]. It has to be demonstrated that even if high Pu contents are reached locally during irradiation (> 0.5), reactor safety is not compromised. The experimental data available in the literature for such high plutonium contents are very limited [BRU11, TRU13, BOH14, VAU14, STR16]. These studies cover a wide range of plutonium contents ($y > 0.75$, $0.15 < y < 0.65$, $0.40< y <0.70$, $0.15< y <0.45$ and $0.14 < y < 0.62$ respectively), but provide limited experimental data and are sometimes incomplete. The critical analysis of these experimental data, by Fouquet-Métivier *et al*., shows that there is a lack of reliable experimental data for $0.5 < y < 0.8$. The melting temperature minimum is also to be expected in this composition range. An accurate knowledge of the thermal properties of U-Pu mixed oxides for Pu/(U+Pu) > 0.45 is thus mandatory. Complementary to the experimental studies, it is also essential to develop theoretical approaches such

as molecular dynamics as it brings data in composition and temperature ranges where the measurements are difficult to perform. These computational methods also provide a better understanding of the thermophysical properties of MOX systems [BAT21] [NJI20] [TAK20]. This bridges the gap between the atomic and the pellet scales.
However, to minimize as much as possible the uncertainties in the measurements, highly homogeneous (elemental and microstructure) samples with Pu contents between 0.60 and 0.70 have to be manufactured. The co-milling process, which is the reference synthesis process for SFR mixed oxide fuels, has already been used in several studies [DUR00, VAU14, VAU15, STA17, MAR17, DAW16, KAT08]. It appears to be the best route to reach high density (> 95% TD) (Theoretical Density), homogeneous chemical distribution of cations (surface fraction of U-rich and Pu-rich agglomerates < 5%), a well-controlled oxygen content (O/M ratio), and a monophasic solid solution. The challenge associated with the manufacturing of such materials is the miscibility gap domain, existing for Pu contents higher than y = 0.17, and O/M ratio ranging between 1.985 and 1.51 in the U-Pu-O phase diagram [PEL20]. As illustrated by Truphemus [TRU13T], entering this domain would lead to the precipitation of secondary phases and to the formation of cracks at the interface. Then, appropriate manufacturing parameters such as sintering temperature and atmosphere, have to be optimized.

This paper describes the optimization of the manufacturing process used for the synthesis of $U_{1-y}Pu_yO_{2-x}$ mixed oxides with high plutonium contents (y = 0.60, 0.65 and 0.70). Experimental results obtained by characterizations at various scales are also presented. Density measurements were performed by two different methods to determine the porosity distribution, i.e. the proportion of open and close porosities. TIMS analyses were realized to determine the U, Pu and Am content. SEM-EBSD (Scanning Electron Microscope – Electron BackScatter Diffraction) mappings were carried out to measure grain size distribution and their orientation. The cationic homogeneity was studied by EPMA (Electron Probe Micro Analysis) measurements. X-ray diffraction (XRD) was also performed in order to determine the structure and the lattice parameters of the oxides, as well as to estimate the O/M ratio. Lastly, µ-Raman spectroscopy measurements were also carried out, in addition to EPMA, to characterize the matrix homogeneity.

2. Experimental

All the experiments were performed in the glove boxes under inert atmosphere (N_2) at the ATALANTE facility of CEA (Marcoule, France).

2.1. Materials

2.1.1. Materials characteristics and powder preparation

Uranium dioxide $UO_{2.11}$ and plutonium dioxide $PuO_{2.00}$ powders were used for the manufacturing of the pellets. The $UO_{2.11}$ powder was obtained using the ammonium di-uranate (ADU) wet chemistry route [MAN12, MAN12-2, MUR01, JAN72]. The particles obtained were atomized and dried in order to finally get spherical agglomerates between 10 and 50 µm. The $PuO_{2.00}$ powder was obtained from the calcination of $Pu(C_2O_4)_26H_2O$ oxalate under air to get parallelepiped-shaped particles size of ~ 15 µm. The synthesis and the characteristics of these powders are fully described in [BER13T]. In this study, three compositions of UO_2/PuO_2 mixtures were prepared with Pu/(U+Pu) = 0.60, 0.65 and 0.70. A direct co-milling process was used. The main goal of the milling phase is to micronize and intimately mix the powders. This step is crucial in order to maximize the homogeneity of the $(U,Pu)O_2$ solid solution after sintering. First, uranium and plutonium dioxide powders were blended together in appropriate ratios (for 30 min with a 0.5 L container rotating at 24 rpm). Then, the mixture was milled during 4 h in a ball mill using metallic U-Ti balls (diameter of 12 mm). The final powder was dry sieved to 200 µm without pre-compaction, in order to remove agglomerates and facilitate the filling of the matrix for pelletizing. For each composition, a batch of 30 g of powder was produced.

2.1.2. Sample shaping

Pellets were shaped using an Osterwalder automatic uni-axial press equipped with a 6 mm diameter floating matrix. For each pellet, 1 gram of powder was pressed leading to 6 mm height cylinders. The pressure applied was constant for all the pellets and equal to 450 MPa, to obtain a satisfactory

mechanical toughness and a relatively homogenous density in the whole green pellet, equal to 63% of TD. Only an external lubrication, with zinc stearate, was used in order to improve pressing performance as well as the green pellet properties.

2.1.3. Sintering and atmosphere control

Sintering was performed using a ECM furnace, which operates up to 2023 K under Ar + 4.3% H_2 + ε vpm H_2O, with a 25 $L.h^{-1}$ flow (flow rate corresponding to 4-5 renewals/hour for the cell atmosphere). To determine the sintering conditions (atmosphere and temperature), leading to monophasic samples with O/M = 2.00, thermodynamic calculations were performed using the Thermo-Calc software [COM23, KAT16, SUN85], with the model derived by Guéneau *et al.* [GUE11] in the TAF-ID database (Thermodynamic for Advances Fuel – International Database version 12) [GUE21].

The oxygen potentials were calculated for each Pu content, as a function of temperature, for several O/M ratio.

The calculations for $U_{0.40}Pu_{0.60}O_{2\pm x}$, $U_{0.35}Pu_{0.65}O_{2\pm x}$ and $U_{0.30}Pu_{0.70}O_{2\pm x}$ are given in Fig 1. a), b) and c) respectively. The red area corresponds to the domain where the mixed oxide is stoichiometric (O/M = 2.000 ± 0.001), while the dashed lines represent the oxygen potential for several moisture contents in the atmosphere: 10, 3500 (or 4000 vpm) and 24000 vpm H_2O. Comparison of these calculations shows that for a fixed moisture content and temperature, the O/M decreases with the Pu content. It corresponds to a tendency towards reduction with increasing Pu content. Thus a higher H_2O content (4000 vpm) was chosen for the 0.70 Pu content sample. Another objective was to maximize the cations diffusion in order to obtain both dense ceramics and the formation of $(U,Pu)O_2$ solid solution. To achieve this goal, a high-temperature thermal cycle with high oxygen potential was preferred [VAU14T, TRU13T]. However at high temperature and in these oxygen potential conditions, the mixed oxide has an O/M ratio lower than 2.000 ± 0.001. In these conditions, two plateau have to be performed to obtain the targeted properties. The first one, at 1973 K, was performed to densify and to form the solid solution. In fact, this high temperature allows the cation diffusion to occur. The second plateau, at 1173 K, is carried out to adjust the final O/M ratio to 2.00. This temperature was chosen as it corresponds to the one for which the O/M ratio is equal to 2.00 for the chosen moisture content (blue mark). The best compromise for the moisture was set to 3500 vpm for the 0.60 and 0.65 Pu contents and 4000 vpm for the 0.70.

As the diffusion mechanisms are slow [GLA84], the duration of the first plateau was optimized. Therefore, several sintering durations were tested (6, 12 and 24 hours) on the first composition (y = 0.60). The density and the formation of the solid solution was controlled by performing XRD, hydrostatic density measurements, EBSD and Raman spectroscopy. For the three durations, the solid solution was formed. The results showed that 24 hours at 1973 K did not lead to significant modifications of the microstructural properties compared to 12 hours. In particular, no de-densification was observed, phenomenon which could have been caused by the long duration of the plateau [BER13T]. After a 6 hours plateau, a 1% decrease in density and a smaller grain size were obtained compared to results obtained with a 24 hours plateau. On this basis, an intermediate duration of 12 hours was finally selected to ensure that the solid solution is fully formed and the pellet reached the targeted density. Considering that the solid solution already formed at 1973 K, the second plateau does not require as much time to reach the thermodynamic equilibrium because it involves only the oxygen diffusion. Then, only a 4 hours holding time was applied. Based on the results obtained with the previous sintering cycle tests for the three Pu contents, the following conditions were chosen:

- An atmosphere with Ar + 4.3 % H_2 with 3500 vpm H_2O for y = 0.60 and 0.65 and 4000 vpm for y = 0.70,
- Heating and cooling ramps of 2°C/min (usually applied),
- A first plateau at 1973 K for 12h (red mark) to form the solid solution. At this point the material is hypo-stoichiometric,
- A second plateau at 1173 K for 4 hours (blue mark) to adjust the oxygen stoichiometry to 2.00.

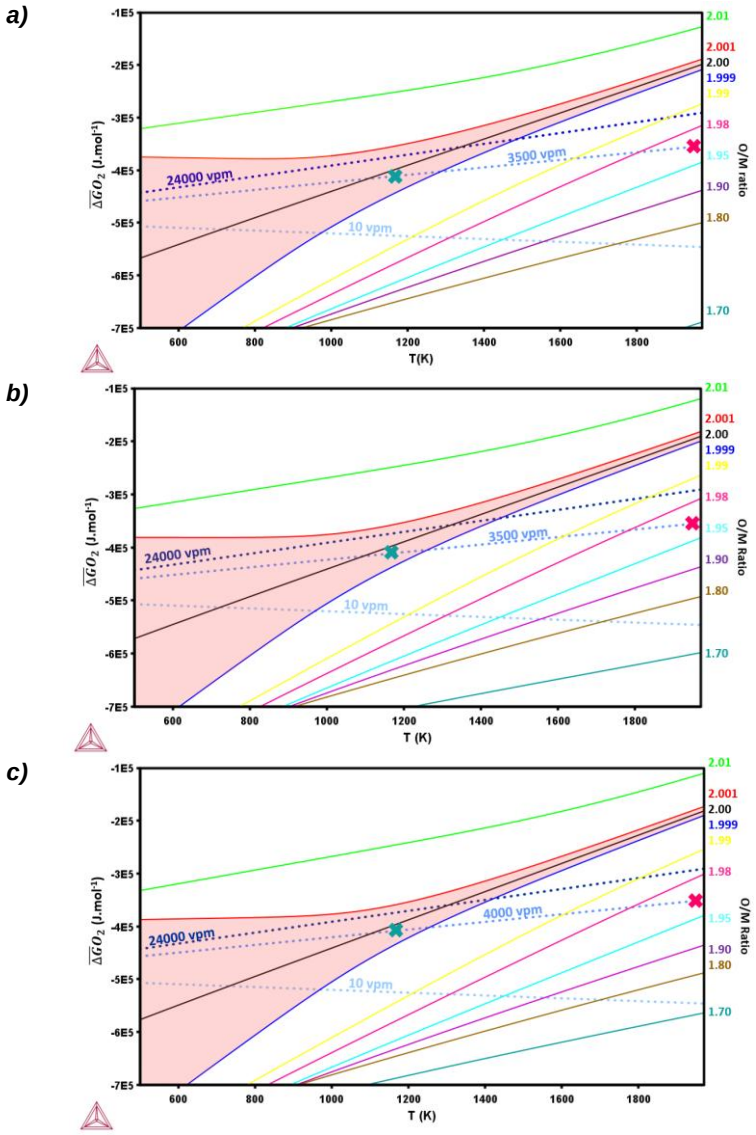

Fig 1. Oxygen potential calculated in function of temperature for different O/M ratio and for a moisture of 10, 3500 or 4000 and 24000 vpm for a) $U_{0.40}Pu_{0.60}O_{2.00}$ b) $U_{0.35}Pu_{0.65}O_{2.00}$ and c) $U_{0.30}Pu_{0.70}O_{2.00}$ mixed oxides.

2.2. Methods

2.2.1. Sample preparation

For each sample, the measurements were performed on a longitudinal cross section cut from a full pellet using a wire saw. The sample was then mechanical polished, up to a mirror finish using Biodiamant MM140 Liquid (Lam Plan) with a granulometry of 0.75 µm. Then, a last step with colloidal silica suspensions (0.2 µm) was used.

2.2.2. EBSD (Electron Back Scattered Diffraction)

SEM observations were performed with a Tescan MIRA 3 microscope equipped with a YAG (Yttrium Aluminium Garnet) BSE (Backscatter Electron) detector and an AMETEKDigiView5 EBSD (Electron Backscatter Diffraction) camera. The intercept method was applied to determine the average grain size [MEN69]. The accelerating voltage is 20 kV, the beam intensity (BI) is 20 with a 3-6 nA extraction current and the spot size is 43 nm with a working distance of 16 mm. Six 309 x 309 µm EBSD maps were carried out (resolution of 441 pixels) to identify, for each grain, its size and orientation matrix thanks to OIM Analysis 8 software. The grain sizes obtained are given in CED (Circular equivalent diameter).

2.2.3. TIMS analyses

Thermal-Ionization Mass Spectrometer (TIMS) analyses were carried out, using a Thermo Fisher Triton and VG Sector 54 mass spectrometer, to obtain the U and Pu mole ratios within the samples. The measurements were collected using Faraday cups coupled to 10^{11} Ω amplifiers. First the powder was dissolved with a mixture of HNO_3/HF (8 mol.L^{-1}/0.05 mol.L^{-1}) at high temperature until total dissolution. A fraction was collected for gamma analysis (Am content) or ICP-MS (cation content). Uranium, Plutonium and Americium were then separated, with a UTEVA resin to determine the isotopy by TIMS. The solution was diluted to obtain a concentration of U reaching 10 mg/L. A ^{235}U enriched tracer was added to measure the U content by the isotopic dilution. By the same way, for the Pu, the solution was diluted to obtained a Pu concentration of 5 mg/L. A ^{242}Pu enriched tracer is added, permitting to determine the Pu content from the isotopy. This technique is detailed by Quemet *et al.* [QUE18, QUE19] and Bürger *et al.* [BUR17].

2.2.4. Density measurements

Density measurements were carried out by two different methods: hydrostatic method and porosity analyses. Three hydrostatic measurements per pellet were performed by immersion in bromo-benzene solution, for a total of 20 pellets for each composition. The theoretical value used for the calculation of the sample density was calculated using the lattice parameters obtained by X-Ray diffraction, assuming that O/(U+Pu) = 2.00. This first method permits the determination of the density and the fraction of open and close porosity. The porosity analyses were also performed using optical microscopy by analyzing the image using FIJI software [SCH12]. Ten images per magnification (10x, 20x, 50x, 100x) were collected from the center and the border of the pellet. Porosities detected in greyscale images are expressed in CED (Circular Equivalent Diameter) after processing. This second method allows the determination of the porosity distribution in our sample in terms of surface fractions and the calculation of the density. The density determined by image analysis is obtained from the percentage of the total porosity area (noted P) by calculating 100-P.

2.2.5. XRD

XRD analyses were performed at ambient pressure and room temperature with a BRUKER D8 Advance diffractometer equipped with a Bruker LynxEye linear detector with a 3° 2θ opening angle. The diffractometer was set in the Bragg-Brentano θ / θ geometry, equipped with a copper source: λ (Kα1 and Kα2) = 1.5406 and 1.5444 Å, respectively.

For each composition, ~ 100 mg of sample were manually co-milled in an agate mortar. Around 25 mg of gold (Alfa Aeser with a purity of 99.96%) were added as an internal reference. The mixture was then dispersed in a polymer grease in order to avoid spreading powder. Further details can be found in Vauchy *et al.* [VAU21]. The diffraction patterns were collected by scanning from 20° to 140° 2θ with a set-interval of 0.1° 2θ and a counting time of 5 seconds per step. For each composition the pattern was collected one week after manufacturing to minimize alpha self-irradiation. The analysis and refinement of the X-ray patterns were performed with the Pawley method [PAW81] using the Bruker TOPAS 6.0 software. The 2θ zero-point deviation was corrected by fixing the lattice parameter of the gold reference to 4.0786 Å (JCPDS # 4-0784).

2.2.6. Raman Spectroscopy

Raman Spectroscopy was carried out using a Horiba Jobin-Yvon iHR320 Raman spectrometer coupled to an optical microscope developed by Optique Peter (Lyon, France). Spectra were systematically recorded using a 100x or 50x objective and a 532 nm wavelength laser, along with a 1200 groove/mm^{-1}. This configuration allows an accuracy of ± 1 cm^{-1} [KAH22]. Light from a neon lamp was injected in the path of the scattered light, to get a permanent frequency calibration of the spectrometer. Spectra were recorded between 90 and 1950 cm^{-1}. The spectrometer was calibrated, using a silicon standard whose Raman line frequency has been fixed at 520.5 cm^{-1}. In order to avoid overheating and/or modification of the sample due to laser illumination, the incident power was adjusted to 0.8-1 mW/μm^2. Data acquisition and treatment were performed with the LabSpec v6.4 software (Horiba). The background was fitted using a fourth degree polynomial function. Each Raman band was subsequently fitted with mixed functions (Gaussian + Lorentzian) of same frequencies and widths, permitting to obtain for each band position, width and intensity. Further details can be found in Kahraman *et al.* [KAH22].

Spectra acquisition was performed along the radius of a longitudinal section of the pellet, as a line. Two spectra with an acquisition time of 30 s were recorded each 1.5 µm, considering that the spatial resolution of the laser is 0.8 μm^2. On the positions of interest spotted (U- or Pu- agglomerates) on the line, mapps were also recorded. The dimensions of the mapping are 50 per 60 µm, and two spectra with an acquisition time of 30 s were recorded each 1.5 µm.

2.2.7. EPMA

Electron Probe Micro Analyses were performed with a CAMECA SX100 device, equipped with a tungsten source and an electron accelerating voltage of 20 kV. PET crystal was used to observed U M_α and Pu M_β peaks and a PC1 (W/Si) multilayer crystal was used for the O K_α peak.
Various types of experiments can be carried out. Prior analyses, the sample was decontaminated and metallized with carbon. First, WDS spectra were acquired in different zones of the samples using a time per step of 200 ms. Also, pseudo-quantitative maps of U, Pu and O distributions were done, with a vertical and horizontal resolution of 1 µm without background subtraction. For this kind of experiment, the cartography surface is 1 mm^2 corresponding to 1024 per 1024 pixels. A current of 150 nA and a time of step of 20 ms were used.

The maps are obtained by comparing the plutonium content from the quantitative measurements and the number of counts in the maps. This allows one to define a function between these two variables. With this method, the plutonium content (% mass) is evaluated in each pixel of the map. However, the uncertainty is high due to the low counting time, approximately 1%. Also, the oxygen maps were not significant, due to a too short counting time. As such, why they are not presented herein.

3. Results

3.1. Microstructure, density and chemical analysis

For each sample, optical microscopy observations of the center of the pellet were performed. As illustrated by Fig 2 a), b) and c), an homogeneous repartition of the porosity was observed and no crack was detected. The density measurements gathered in Table 2, show that values higher than 95% TD are obtained for each composition, while similar values were also determined by image analysis from optical microscopy data. The theoretical value used for the calculation of the sample density was calculated using the lattice parameters from X-Ray diffraction, corresponding to 11.38, 11.42 and 11.45 for each composition (0.60, 0.65 and 0.70 Pu/(U+Pu)) respectively. These microstructures indicate that the sintering was well optimized, allowing to reach high relative density. A decrease of the density can also be seen with increasing plutonium content, as well as the closed porosity fraction. This decrease in density with increasing Pu content has already been observed by Kutty et al [KUT00]. No clear explanation is given by the authors to explain this observation. However it could be due to an increase of the Pu diffusion coefficient with the Pu content in the MOX. This would be consistent with the model of Chakraborty *et al.* [CHA20] that shows a significant increase of the Pu diffusion coefficient above 40 % Pu, based on their DICTRA model. Netherless there are no experimental data of diffusion coefficient in this Pu composition range for an O/M equal to 2 to support this assumption. New measurements would be very useful to understand this phenomenom. The associated porosity size distributions are shown in Fig 3, by the evolution of the cumulative surface fraction. The same trend can be observed in the distribution of porosity for the three compositions studied. Indeed, porosities smaller than 1 µm represent only 10% of the total surface fraction, for each composition. Between 1 and 10 µm, this corresponds to 85% of the total surface fraction depending on the Pu content (a bit lower for 0.60 Pu contente).

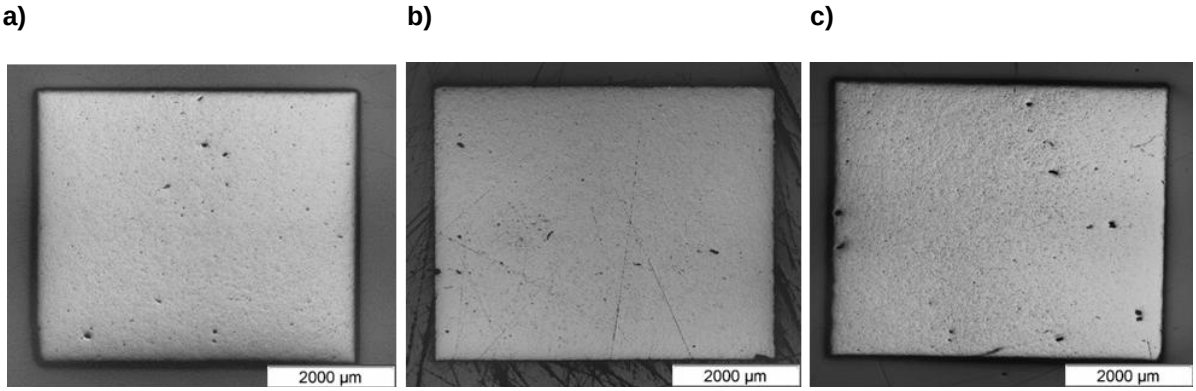

Fig 2. Optical macrograph of the sintered pellets a) $U_{0.40}Pu_{0.60}O_{2.00}$, b) $U_{0.35}Pu_{0.65}O_{2.00}$ and c) $U_{0.30}Pu_{0.70}O_{2.00}$.

Table 1. Densities measurements carried out by hydrostatic method compared to the image analysis.

y	TD[1] ($g.cm^{-3}$)	%TD Hydrostatic method	% Open porosity	% Close porosity	%TD from image analysis
0.60	11.38	97.0 ± 0.1	0.3 ± 0.1	2.7 ± 0.1	96.6 ± 1.1
0.65	11.42	96.0 ± 0.1	0.4 ± 0.1	3.6 ± 0.2	96.5 ± 1.0
0.70	11.45	95.8 ± 0.1	0.2 ± 0.1	4.0 ± 0.2	95.1 ± 1.4

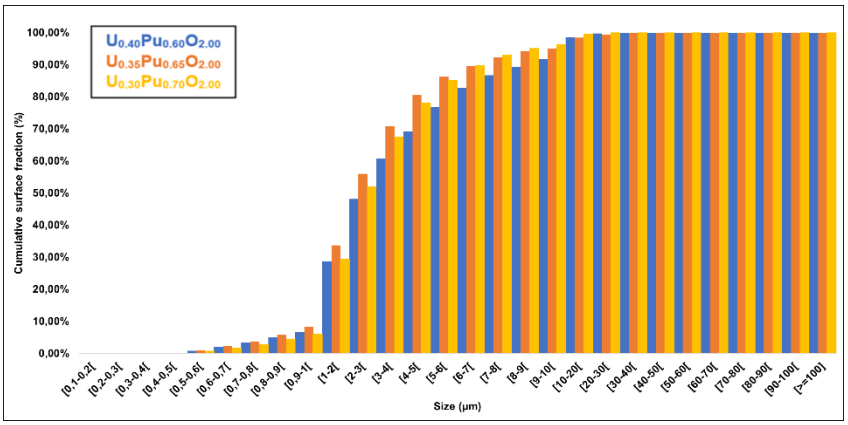

Fig 3. Cumulative surface fraction of the porosity size distribution in $U_{1-y}Pu_yO_{2.00}$ samples: y = 0.60 (blue), 0.65 (orange) and 0.70 (yellow).

For each composition, six EBSD maps were collected randomly. An example of EBSD map collected for each composition is shown in the Fig 4 a) b) and c). In total 2914, 2507 and 3504 grains were counted for Pu content of 0.60, 0.65 and 0.70 respectively. The grain size distributions obtained are shown in Fig 5, and the average grain sizes (given in CED) extracted from the SEM-EBSD maps are summarized in Table 2. The same grain size distribution is observed for the three compositions, however a smaller grain size is observed for the last composition (0.70 Pu/(U+Pu)). Indeed, for 0.60 and 0.65 Pu/(U+Pu), 50% of the grains are smaller than 12 µm. Then, for the 0.70 Pu content, 50% of the grains are smaller than 15 µm. However, their distribution remains homogeneous. Granular growth occurs during sintering, when densification and inter-diffusion of cations are achieved. The highest plutonium content, which reveals a smaller grain size, also revealed a lower density. These elements suggest that granular growth was lower than for the other two Pu contents. Grain size evolution can be described by a monotonic function of relative density, as shown by Simeon, this can be explained by different sintering trajectories [SIM22T], justifying this difference. This sintering trajectory represents the evolution of grain size as a function of relative density during the sintering of a polycrystalline

[1] Theoretical density calculated with the lattice parameters.

compact. And each sintering trajectory is unique. It is associated with a given material, powder production conditions, shaping process and sintering device.

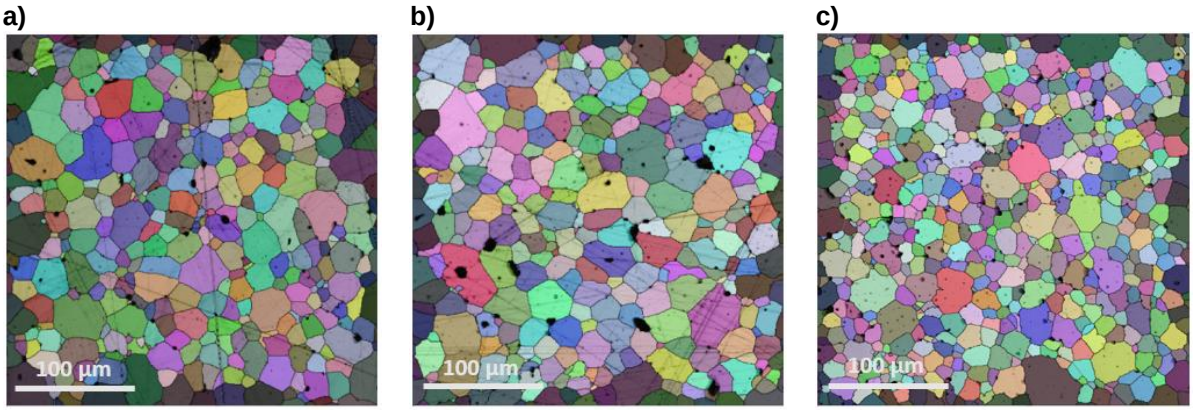

Fig 4. EBSD maps of the sintered pellets a) $U_{0.40}Pu_{0.60}O_{2.00}$, b) $U_{0.35}Pu_{0.65}O_{2.00}$ and c) $U_{0.30}Pu_{0.70}O_{2.00}$.

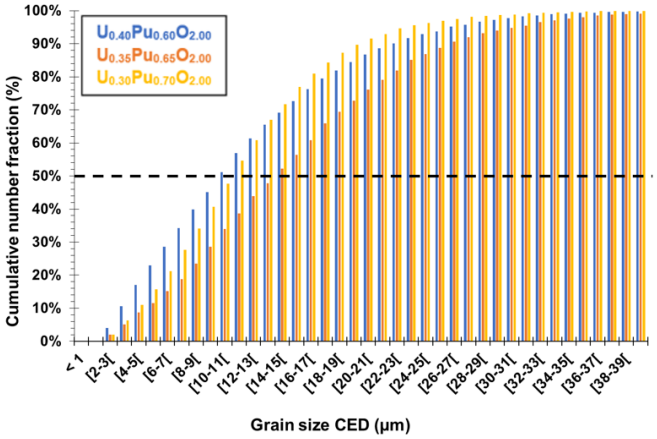

Fig 5. Grain size distribution in $U_{1-y}Pu_yO_{2.00}$ samples: y = 0.60 (blue), 0.65 (orange) and 0.70 (yellow).

Concerning the samples composition, results from TIMS analyses are summarized in Table 2. The plutonium contents are consistent with expected values, although slightly lower (< 3%), which was attributed to matter loss during the blending step. The americium content was also measured and an (Am/(Pu+Am)) ratio of 0.01 was determined. This americium comes from the beta decay of ^{241}Pu. As the same PuO_2 powder was used for their fabrication, the Am/(Pu+Am) % is the same for the three batches prepared. This Americium content is not taken into account in the results of this study, as it is negligible.

Table 2. Plutonium content (y= Pu/(U+Pu)) determined by chemical analysis and grain size average.

y	Pu/(U+Pu) from TIMS[2]	Average Grain size (µm)	CED average weighted by surface (µm)
0.60	0.59 ± 0.02	12 ± 1	21 ± 1
0.65	0.63 ± 0.02	16 ± 1	24 ± 1
0.70	0.69 ± 0.02	12 ± 1	18 ± 1

3.2. EPMA

[2] Thermal Ionization Mass Spectroscopy

For each composition, pseudo quantitative plutonium mappings are shown in Fig 6. a), b) and c). The color scale corresponds to the plutonium content (i.e. Pu/U+Pu wt %), while the grey points account for the porosities. Some uranium-rich agglomerates and enriched-plutonium hot spots can be observed in green/yellow and red/purple respectively. The size of the uranium-enriched agglomerates are around 50 µm in diameter. In the plutonium hot spots, the maximum plutonium content reached as high as 85 Pu/(U+Pu) wt.%. The sizes of these clusters are around few tens of microns.

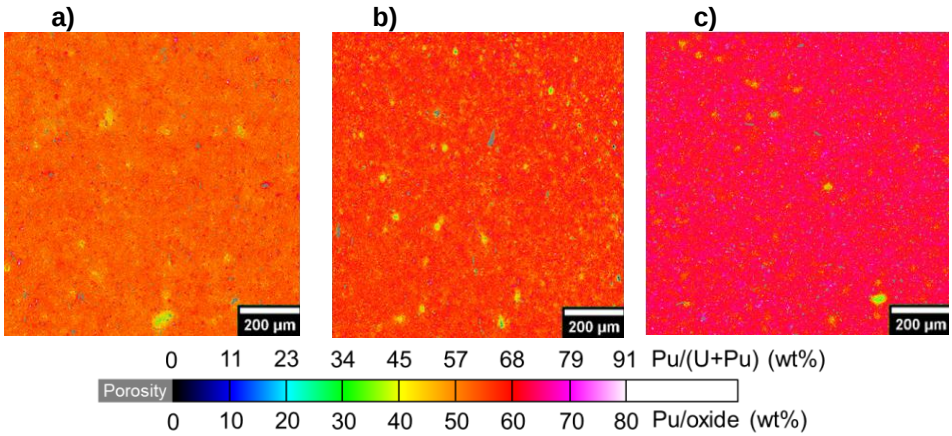

Fig 6. Pseudo quantitative plutonium mapings carried out by EPMA for a) $U_{0.40}Pu_{0.60}O_{2.00}$ b) $U_{0.35}Pu_{0.65}O_{2.00}$ c) $U_{0.30}Pu_{0.70}O_{2.00}$ mixed oxides with the color scale corresponding to the plutonium content (Pu/U+Pu).

The plutonium statistical distributions extracted from EPMA mapping are plotted in Fig 7. A mono-modal distribution is observed for the three compositions. The latter can be fitted using a Gaussian function. The values obtained given in Table 3 correspond to the average plutonium content of the matrix phase, that explains the gap with the plutonium content determined by chemical analyses (Table 2), which refers to the whole sample. The widths of the distribution (shown on the Table 3), corresponding to a 2σ confidence interval, are very similar or equal, depending on the composition. This result suggests that the Pu content is constant in the matrix.

The surface fractions of the U-agglomerates and Pu hot spots were determined by calculating their areas, for the range of interest (corresponding to the beginning and the end of the Gaussian curves): it corresponds to ± 10 wt% Pu/(U+Pu) (against the average Pu content), i.e. outside the ± 2σ interval. The latter corresponds to a 95% probability of having a value within the interval according to the normal distribution. These results are summarized in the Table 3. For each composition, U-rich and Pu-rich agglomerates are evidenced and the resulting proportions are equal to less than 5 % of the sample. Finally, the results show a homogenous plutonium distribution within the matrix.

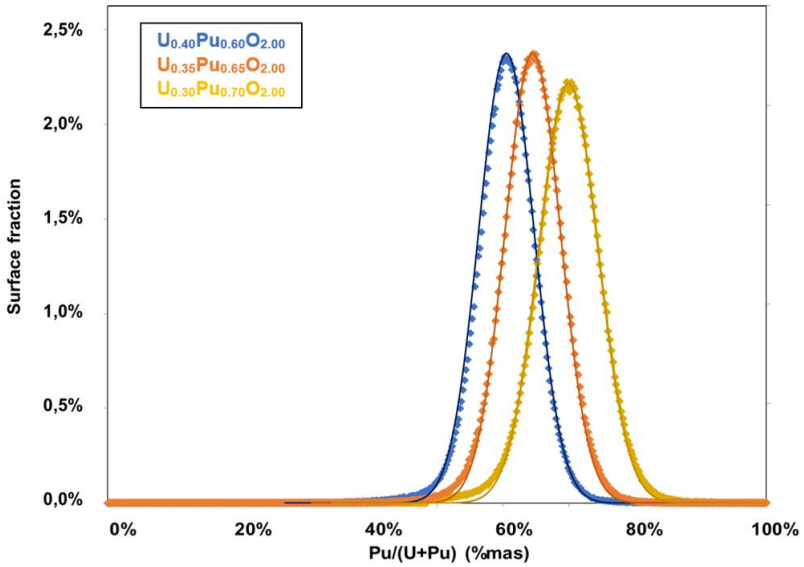

Fig 7. Gaussian surface distribution of the Pu content for our $U_{1-y}Pu_yO_{2.00}$ samples: y = 0.60 (blue), 0.65 (orange) and 0.70 (yellow).

Table 3. Pu contents and surface proportion of U-rich agglomerates determined by EPMA

Composition	Pu content of the matrix (y=Pu/U+Pu)	U-rich agglomerates (surf.%)	Pu-rich agglomerates (surf.%)	Width of the Gauss curve
$U_{0.4}Pu_{0.6}O_2$	0.60 ± 0.01	1.7 %	1.6 %	9.89 ± 0.08
$U_{0.35}Pu_{0.65}O_2$	0.63 ± 0.01	2.6 %	1.1 %	9.89 ± 0.08
$U_{0.3}Pu_{0.7}O_2$	0.70 ± 0.01	2.9 %	1.9 %	10.60 ± 0.08

3.3. XRD

The diffraction patterns were collected for the three compounds, and are shown in Fig 8. For each sample, only one Fm-3m phase exhibiting a single fluorite-type structure is detected, as illustrated by Fig 8-b, and the lattice parameters determined are given in Table 4. From this lattice parameter, the O/M ratio was calculated thanks to the Duriez *et al.* law [DUR00]. The relation is defined by the Equation 1 where y is the plutonium content and x the deviation from the stoichiometry (O/M=2.00). This describes the variation of the lattice parameter between $UO_{2.00}$ (5.470 Å [LEI15]) and $PuO_{2.00}$ (5.396 Å [GAR65]), corresponding to the Vegard law. However this relation is validated for y < 0.45 and O/M > 1.819.

Equation 1 $$a(U_{1-y}Pu_yO_{2-x})\ \text{Å} = 5.470 - 0.074y + 0.34x$$

The O/M ratio calculated for each composition are summarized in Table 4, where the plutonium content determined by EPMA is used. The results show all the 3 samples are monophasic solid solutions with O/M ratio equal to 2.00. Moreover, the deviation of the results obtained from the Vegard law is less than 0.05 %, which is negligible.

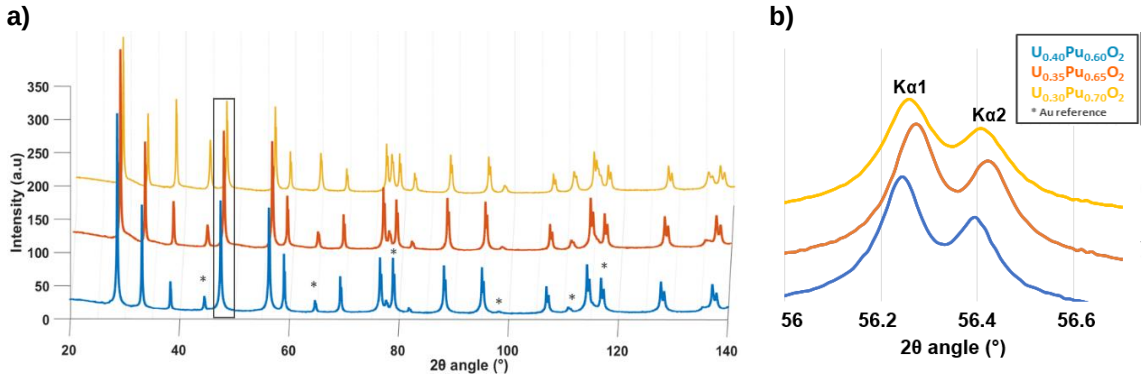

Fig 8. XRD Patterns recorded for each sample a) full patterns between 20 and 140 ° 2θ b) Magnification of the (311) peak of the fcc structure.

Table 4. Structure and lattice parameters of the $(U_{1-y}Pu_y)O_2$ compounds.

Pu content (Pu/(U+Pu)	**0.595** ± 0.051	**0.629** ± 0.052	**0.704**± 0.056
Space group	Fm-3m	Fm-3m	Fm-3m
Lattice parameter (Å)	5.426 ± 0.001	5.424 ± 0.001	5.419 ± 0.001
Deviation from Vegard law [SAR70]	0.00%	0.02%	0.02%
O/M ratio from Duriez *et al.* law [DUR00]	2.000 ± 0.004	1.998 ± 0.004	1.997 ± 0.004

3.4. Raman Spectroscopy

2000 spectra were collected each 1.5 microns along a 3 mm line on the 3 samples. These spectra were averaged and are compared in Fig 9 a). They are almost identical with one main band around ~460 cm^{-1} and a second large band at ~575 cm^{-1}. Such spectra are typical of a fluorite type structure like UO_2, PuO_2 and $(U,Pu)O_2$ [MED20, ELO16, ELO17]. In such structure, according to the group theory, only one triply degenerated mode T_{2g} is allowed in Raman. Its position (445 cm^{-1} for $UO_{2.00}$ and 478 cm^{-1} for $PuO_{2.00}$ [ELO16, ELO17, MED20, NAJ17, SARS12, VIL21]), is directly linked to the plutonium content and the O/M ratio for $(U,Pu)O_2$ compounds as shown by Medyk *et al*. [MED20]. The increase in Pu content induces a reduction of the lattice parameter. The width of the T_{2g} band depends directly of the structural disorder, crystallite size and plutonium content, but it has not been studied in our case. The positions of the T_{2g} band are reported in Table 5. Considering that the solid solution studied are stoichiometric, as determined by XRD, the equation determined by Medyk *et al.* could be used for the determination of the plutonium content [MED20]. This equation has been validated for a Pu content lower than 0.45, and is described by the Equation 2, with w the T_{2g} band position and the constants k_1, k_2 and k_3 equal to -28.2 ± 1.0 $cm^{1/2}$, 485.7 ± 1.9 cm^{-1} and 180.0 ± 8.4 respectively. The results are summarized in the Table 7 where the deviation from the EPMA results is also given. This deviation is less than 6% from the plutonium content determined by EPMA.

Equation 2

$$\%Pu = k_1 * \sqrt{k_2 - w} + k_3$$

The large band at ~575 cm^{-1} corresponds to the 1LO mode with its two shoulders slightly observable around 535 and 630 cm^{-1}. Such group of bands are depicted as the triplet defect band U* or U^1, U^2 and U^3 triplet in the literature [KAH22]. The main band, 1LO mode corresponds to an infra-red mode, and its activation can be explained by the loss of the inversion center in the lattice caused by the disorder (structural and/or chemical) induced by the substitution of uranium by plutonium in the UO_2 structure. The origin of the two shoulders on both sides of the 1LO mode for $(U,Pu)O_2$ compounds is still being discussed in the literature [MAS17, TAL17, TAL18, DES11, DES12, MED20, ELO17, LIV06, LIV22, BOH14, LIV16,VIL21] .

In a fluorite-type structure, a second order mode (2LO) is allowed in Raman and is located around 1150 cm^{-1}. With a 532 nm laser, which is the case here, this mode is strongly resonant for $UO_{2.00}$ and its intensity quickly decreases as plutonium content increases [ELO17]. In our case, as the plutonium

content is very high, this band is not visible. Thus the spectra shown in Fig 9 a) are in the range 100 and 800 cm^{-1}.

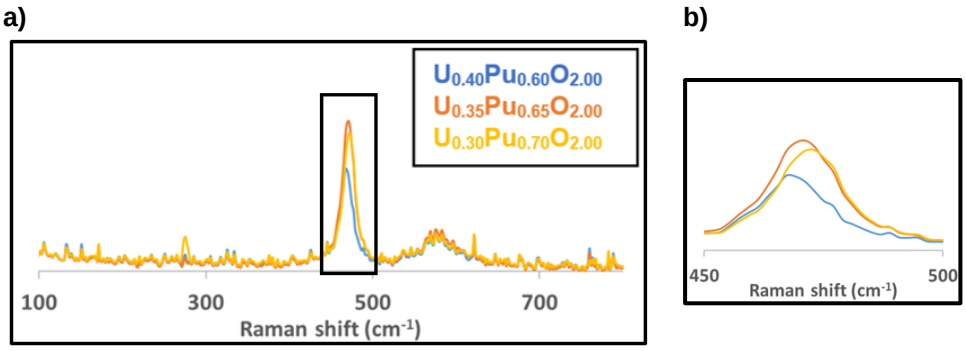

Fig 9. a) Raman Spectra between 100 and 800 cm^{-1} b) T_{2g} position shift from the spectra of the $(U_{1-y}Pu_y)O_2$ compounds between 450 and 500 cm^{-1}.

Table 5 T_{2g} band positions of the samples and Plutonium content estimated.

	$U_{0.4}Pu_{0.6}O_2$	$U_{0.35}Pu_{0.65}O_2$	$U_{0.3}Pu_{0.7}O_2$
Average of the T_{2g} position (cm^{-1})	467.5 ± 0.3	469.4 ± 0.3	471.0 ± 0.3
Pu/U+Pu estimated for O/M=2.00 [16]	0.61 ± 0.03	0.67 ± 0.03	0.73 ± 0.03
Deviation from EPMA	2 %	6 %	5 %

Along the line analysed, some Raman spectra exhibited T_{2g} band positions close to UO_2 at 445 cm^{-1} [BEG90, DES12, MAR66, TAL15]) or PuO_2 at 478 cm^{-1} [BEG90, NAJ17, SAS12, VIL19]. Around these locations, Raman maps (50 x 60 μm^2) with 1.5 µm step were performed. From spectra collected on each points of the Raman cartography, T_{2g} band position was determined. These values are transposed in plutonium content, using Medyk *et al.* relation [MED20] and leading to the images shown in Fig 10. Plutonium-rich spots are observed, between 5 and 25 µm maximum diameter, corresponding to the green area for the sample with a Pu content of 0.60 and to the yellow/red area for the 0.65 and 0.70 Pu/(U+Pu) contents. The plutonium hot spots observed by EPMA are about a few tens of microns, which is in the same range.

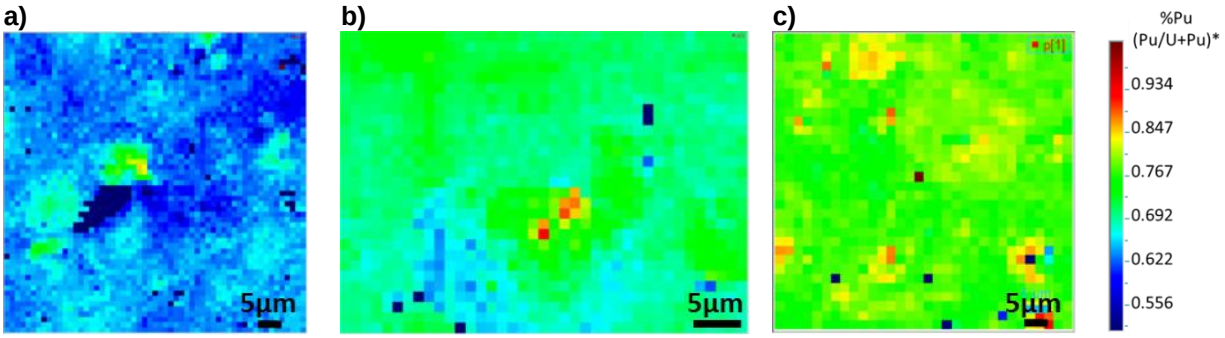

Fig 10. µ-Raman Spectroscopy mapping for a) $U_{0.40}Pu_{0.60}O_{2.00}$ b) $U_{0.35}Pu_{0.65}O_{2.00}$ c) $U_{0.30}Pu_{0.70}O_{2.00}$.

The plutonium distributions histograms were extracted from Raman spectroscopy maps, and plotted in Fig 11. A mono-modal distribution can be observed for the three compositions studied and is fitted using a Gaussian function. The position of this main mode corresponds to the average plutonium content of the matrix phase. However, for both Pu/(U+Pu) = 0.65 and 0.70, deviation from a Gaussian distribution can be seen which makes sense with the Raman Pu mapping shown in Fig 10. Where some agglomerates can be observed, with the color change (directly related to the Pu content). The methodology used for EPMA data was applied for Raman for the calculation of surface fractions. Pu content (y=Pu/U+Pu) values below 0.55, 0.60 and 0.65 are attributed to U-agglomerates, and points

above 0.70, 0.75 and 0.80 correspond to Pu hot spot, for each composition respectively. The data obtained are summarized in Table 6.

On the plutonium histogram distribution, for the composition $U_{0.35}Pu_{0.65}O_{2.00}$, a shoulder was observed for low plutonium content, characteristic of the presence of U-rich agglomerates. This was confirmed by a surface fraction of 1.33 %, higher than for the two other compositions. For the $U_{0.3}Pu_{0.7}O_{2.00}$ sample, a shoulder on high plutonium content was observed, characteristic of the Pu hot spot, confirmed by a surface fraction of 4.92 %.

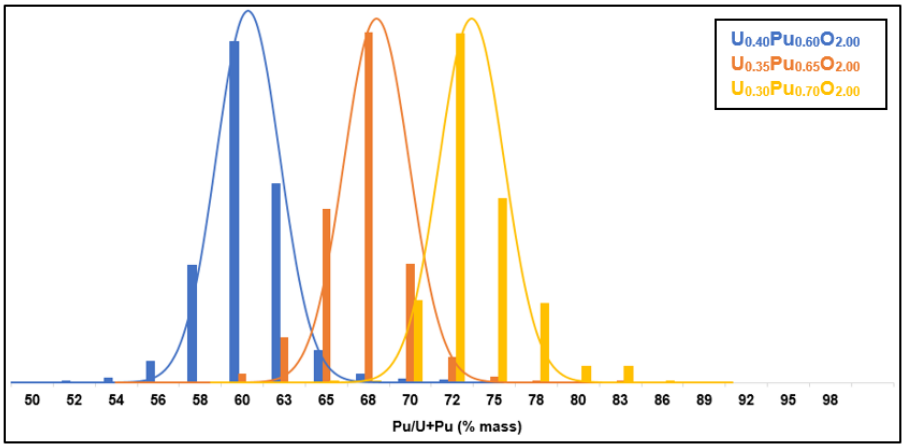

Fig 11. Gaussian surface distribution of the Pu content for our compounds from Raman spectroscopy mapping.

Table 6. Pu contents and surface proportion of U-rich agglomerates determined by Raman spectroscopy mapping.

Composition	Average T_{2g} position (cm^{-1})	y=Pu/(U+Pu) content of the matrix	U-rich agglomerates (surf.%)	Pu-rich agglomerates (surf.%)
$U_{0.4}Pu_{0.6}O_2$	467.9 ± 0.7	0.60 ± 0.03	0.95 %	1.23 %
$U_{0.35}Pu_{0.65}O_2$	469.7 ± 0.7	0.66 ± 0.03	1.33 %	1.78 %
$U_{0.3}Pu_{0.7}O_2$	471.5 ± 0.8	0.72 ± 0.03	0.57 %	4.92 %

4. Discussion

Table 7 summarizes the results obtained with the different multi-scale characterization techniques carried out and presented previously. These results show some differences, especially for the plutonium content. However, if uncertainties are taken into account, the results are in good agreement. The objective of this discussion section is to confront the results, in order to conclude about the chemical cationic distribution, and the O/M ratio of the sample and to highlight the complementarity of the different methods.

Table 7. Synthesis of the results obtained by the multi-scale characterizations to determine the final composition of the manufactured oxides.

	$U_{0.40}Pu_{0.60}O_{2.00}$	**$U_{0.35}Pu_{0.65}O_{2.00}$**	**$U_{0.30}Pu_{0.70}O_{2.00}$**
Chemical analysis	0.59 ± 0.02	0.63 ± 0.02	0.69 ± 0.02
EPMA	0.60 ± 0.01	0.63 ± 0.01	0.70 ± 0.01
Raman line for (O/M = 2.000)	0.61 ± 0.03	0.67 ± 0.03	0.73 ± 0.03
Raman mapping (O/M = 2.000)	0.60 ± 0.03	0.66 ± 0.03	0.72 ± 0.03

Final composition	$U_{0.409}Pu_{0.591}O_{2.000}$	$U_{0.369}Pu_{0.631}O_{1.998}$	$U_{0.311}Pu_{0.689}O_{1.997}$

4.1. Chemical distribution of the plutonium

Global chemical analysis gives the overall plutonium content of our sample, which is less than 3% from the targeted content, but no evaluation of the local homogeneity of the samples. Conversely, EPMA and Raman spectroscopy are two complementary techniques providing data on local Pu/(U+Pu) content.

On the one hand plutonium mapping performed by EPMA, presented in Fig 13, brings information on the matrix homogeneity on a 1 mm^2 scale. On those maps the grey area corresponds to the porosity, and the yellow/green area to local depletion of the considered element (30 µm maximum in diameter). The distribution curves of the Pu repartition calculated and shown on the Fig 7 reveal a mono modal distribution. This mode corresponds to the plutonium content of the sample and the values are summarized in Table 7.

For comparison, the plutonium distribution of a MIMAS sample, $U_{0.90}Pu_{0.10}O_{2.00}$, is plotted with the distribution of our samples (in green Fig 13). These results were published by Kahraman *et al.* [KAH22]. This kind of MOX was produced by two-step process of blending and milling UO_2 and PuO_2 powders, followed by a dilution with UO_2 to reach the targeted U/Pu ratio. During the sintering, only a partial interdiffusion occurs, due to the contact between the micronized UO_2 and PuO_2 particles. Therefore, a $(U,Pu)O_2$ solid solution with variable Pu contents is obtained, composed by matrix, U-rich agglomerates and Pu-rich agglomerates. All the characteristics of this sample are detailed on [KAH22]. This means that the distribution of this type of mixed oxide is multi-modal, which is representative of an heterogeneous material. In total three different modes have been observed with y = 0.01, 0.09 and 0.29. Moreover, the width distribution of the U-rich agglomerates, at 1 wt. %, suggests that the plutonium content is heterogeneous in these agglomerates as well. However, it is of course wider due to the different static of the count. The same observation is made for the plutonium agglomerates mode, at y = 0.29. This kind of distribution is representative of heterogeneous distribution, whether it is for the global homogeneity or in the agglomerates themselves, as shown on the pseudo-quantitative mapping given in Figure 12. This multi-modal distribution is the opposite of what is observed in the case of our samples. Indeed, a mono-modal distribution is observed for the three compositions studied. This way, we can conclude that a global homogeneity of the matrix of our samples is observed.

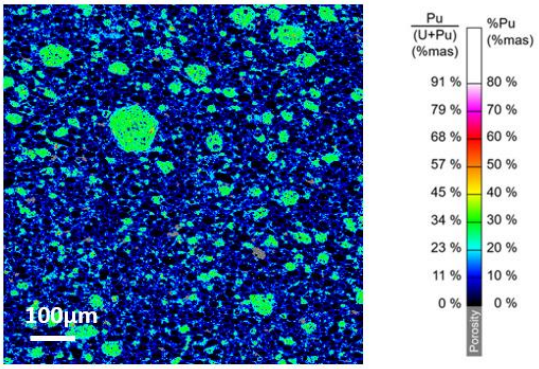

Figure 12. Pseudo quantitative plutonium mapings carried out by EPMA for $U_{0.90}Pu_{0.10}O_{2.00}$ mixed oxides (MIMAS) with the color scale corresponding to the plutonium content (Pu/(U+Pu)) [KAH22].

On the other hand, µ-Raman spectroscopy mapping were also performed to evaluate the local homogeneity, at grain and agglomerate scales. The mapping presented in the Fig 10 shows Pu depleted area as well as hot spots. The corresponding plutonium distributions are presented in Fig 13 for each composition. As for the EPMA results, the plutonium distribution is mono modal. However, a slight shoulder towards the high plutonium content is observed, corresponding to the hot spots visible on the mapping. The comparison between the global (EPMA) and the local (Raman) plutonium

distributions obtained, shows a shift of the average value for the highest Pu contents studied, i.e. 0.65 and 0.70. In fact, this bias was also observed between the targeted plutonium content and the value calculated by the equation of Medyk *et al.* [MED20]. It may be explained by the size difference of the mapping between the two methods: 1 mm^2 for EMPA and 0.03 mm^2 for Raman. Furthermore the Raman mapping were centered on hot spots, as this technique allows to explore local homogeneity (at the agglomerates scale), explaining the difference on the plutonium content average. Thus, it can also be assumed that these hot-spots are not homogeneously distributed within the pellet. Furthermore, taking into account the uncertainties of each experimental technique, it can be concluded that the results are in good agreement. Raman also shows that Pu is homogeneously distributed within the agglomerates.

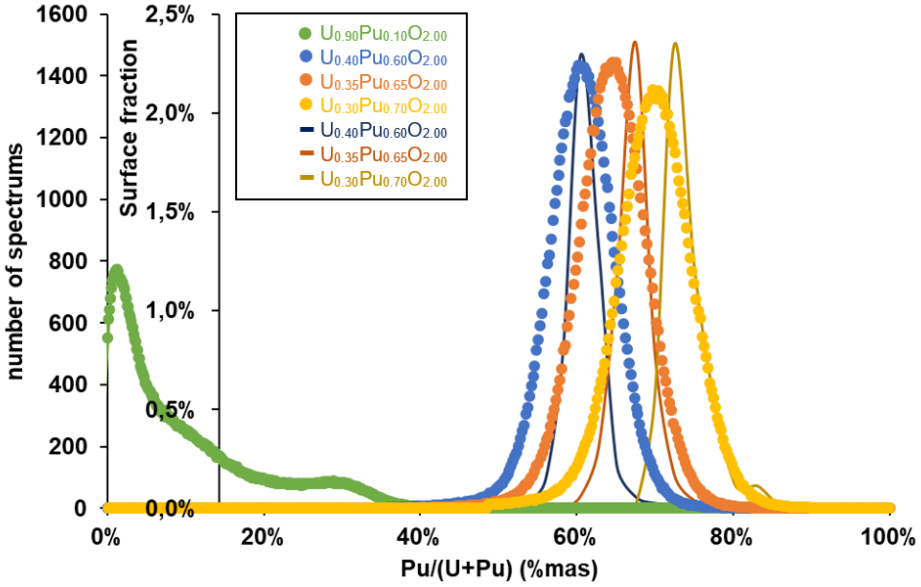

Fig 13. Comparison between the Pu distribution from EPMA (dots) and µ-Raman spectroscopy (lines) for $U_{0.40}Pu_{0.60}O_{2.00}$ (blue) $U_{0.35}Pu_{0.65}O_{2.00}$ (orange) $U_{0.30}Pu_{0.70}O_{2.00}$ (yellow) and MIMAS sample (green).

The results obtained bring to light the complementarity of the methods used: EPMA and µ-Raman spectroscopy, permitting to measure the global (at the sample scale) and local homogeneity (at the agglomerate scale) of the chemical cations distribution, and the importance of using them jointly for a complete analysis.

4.2. Determination of the O/M ratio

The O/M ratio of the matrix was determined by the Duriez *et al*. [DUR00] equation, from the lattice parameter obtained by XRD patterns refinement. In our case this relation could be used because the patterns were collected one week after manufacturing, so there are negligible effects of self-irradiation (inducing a lattice swelling). The lattice parameters determined and the deviation from the Vegard law (where the O/M is equal to 2.00) are summarized on the Table 4. Even if this relation is validated for y < 0.45 and O/M > 1.819, the deviation is lower than 1% for each composition. This allows the validation of the calculated O/M ratio of our material, and the extension of the validated Pu content range for this equation. Also, µ-Raman spectroscopy can also be used to determine the O/M ratio [MED20]. The Equation 3 permit to determine the lattice parameter from the T_{2g} band position (for an O/M ratio equal to 2.00).

Equation 3

$$a(\text{Å}) = h_1 * \sqrt{h_2 - w} + h_3$$

With a the lattice parameter, w the T_{2g} band position (cm^{-1}), and the constants h_1, h_2 and h_3 equal to (1.861 ± 0.040) x $10^{-2} cm^{1/2}$ Å, 482.1 ± 1.0 cm^{-1} and 5.357 ± 0.002 Å respectively. The lattice parameter obtained from XRD and Raman are summarized on the Table 8. The deviation between the both methods is less than 0.1%. The variation between the results of these methods can be explained by

the fact that XRD provides the nature of the crystal lattice, while the existence and shape of the Raman bands in a spectra represent the vibrations of the bonds of the material.

Table 8. Lattice parameters and O/M ratio determined by XRD and Raman spectroscopy.

Pu content (Pu/(U+Pu) from EPMA	**0.595** ± 0.051	**0.629** ± 0.052	**0.704** ± 0.056
Lattice parameter XRD (Å)	5.426 ± 0.001	5.424 ± 0.001	5.419 ± 0.001
O/M Duriez *et al.* law	2.000 ± 0.004	1.998 ± 0.004	1.997 ± 0.004
Lattice parameter Raman (Å) (O/M=2.00)	5.428 ± 0.006	5.423 ± 0.006	5.419 ± 0.006
Deviation	0.04%	0.02%	0.00%

5. Conclusions

This work was devoted to bring into light the complementary of multi-scales characterizations of the structural and microstructural properties of Uranium-Plutonium mixed oxides with high contents of plutonium. The three compositions (y equal to 0.60, 0.65 and 0.70) studied were successfully manufactured by the optimization of the co-milling process conditions.

Dense pellets were obtained, with a density higher than 95% TD. The density was measured by two methods, immersion and image analyses, and the results show a good agreement. The required microstructure was also reached, with a homogeneous distribution porosity and grain size within the pellets.

EPMA and µ-Raman spectroscopy measurements revealed the global and local homogeneity for the plutonium distribution respectively. EPMA mapping shows a mono-modal distribution and a small proportion of agglomerates (< 5 % surface fraction). Raman spectroscopy line and mapping show the presence of hot spots, observed on the mono-modal distribution of plutonium by the presence of a shoulder towards the high content. The comparison of these results with the calculated plutonium distributions highlights the importance of performing multi-scales characterizations. To conclude, an homogenous distribution of cations on the matrix was observed from the EPMA mapping (1 mm^2), as well as at grain and agglomerate scales from the µ-Raman spectroscopy mapping (0.003 mm^2).

The XRD patterns and the Raman spectra, for each composition, confirm the formation of monophasic solid solutions with a fluorite structure. Thanks to the Duriez *et al.* equation, the O/M ratio was determined. For all plutonium contents, all are stoichiometric (O/M = 2.00). Unfortunately, the global distribution, by EPMA, of the O/M ratio along the pellet could not be determined. The oxygen maps were not significant, due to a too short counting time. Moreover, the µ-Raman spectroscopy can also be used to determine the O/M ratio using Medyk *et al.* [MED20]. However, the different laws used in this work are currently valid up to y=0.45, these works highlight a good agreement with them for Pu contents higher than 0.6, suggesting an extension of the ranges of validity.

To conclude, this work demonstrates the interest in carrying out multi-scale characterizations, as well as coupling them.

6. Acknowledgment

The authors would like to thank Camille-Marie Aloin, Méghan Alibert, Lise Barnouin, Mathilde Pons Guillaume Gabriel, Patrice Signoret, Loic Picard and Olivier Miollan for their contributions to the experiments. This research is carried out as part of the European PuMMA project (Plutonium Management for More Agility) which has received funding from the European Union's Horizon 2020 (grant agreement No 945022).

7. References

[BAT21] D. Bathellier *et al*., *J. of Nucl. Mater.*, 2021, vol. 549, p. 152877.
[BEG90] G.M. Begun *et al*., *J. Common Met*., 1990, vol. 162, p. 129–133.
[BER13T] S. Berzati*, thesis*, Influence du potentiel d'oxygène sur la microstructure et l'homogénéité U-Pu des combustibles $U_{1-y}Pu_yO_{2+x}$, Université Bordeaux 1, 2013.
[BOH14] R. Böhler *et al., J. Nucl. Mater*., 2014, vol. 448, p. 330-339.
[BRU11] F. De Bruycker *et al*., *J. Nucl. Mater.,* 2011, vol. 419, p. 186-193.

[BUR17] S. Bürger *et al., Sector Field Mass Spectrometry for Elemental and Isotopic Analysis*, 2017, Ch. 14, p. 381-438.
[CHA20] P. Chakraborty et al., Solid State Ionics, 2020, vol. 357, p. 115503.
[COM23] Computational Materials Engineering, Thermo-Calc software, 02/012023, https://thermocalc.com/
[DAW16] R. Dawar *et al., J. Nucl. Mater.*, 2016, vol. 473, p. 131-135.
[DES11] L. Desgranges *et al*., Inorg. Chem., 2011, vol. 50, p. 6146.
[DES12] L. Desgranges *et al*., *J. Raman Spectrosc*., 2012, vol. 43, p. 455–458.
[DUR00] C. Duriez *et al., J. Nuc. Mat.,* 2000, vol. 277, p. 143–158.
[ELO17] J.M. Elorrieta *et al*., *J. Nucl. Mater.*, 2017, vol. 495, p.484-491.
[ELO16] J.M. Elorrieta *et al*., *Phys. Chem.*, 2016, vol. 18, p. 28209–28216.
[FOU23] P. Fouquet-Métivier *et al.*, Calphad, 2023, vol. 80, p.102523.
[GAR65] E. R. Gardner *et al*., *J. of Inor. and Nucl. Chem*., 1965, vol. 27, p. 541–551.
[GLA84] D. Glasser-Leme *et al*., *Solid State Ionics*,1984, vol.12, p. 217-225.
[GUE11] C. Guéneau *et al*., J. Nucl. Mater., 2011, vol. 419, p. 145-167.
[GUE21] C. Guéneau *et al*., Calphad, 2021, vol. 72, p. 102212.
[GUEN12] C. Guéneau *et al., Comp. Nucl. Mater*., 2012, vol. 2 chap. 02, p. 21-59.
[JAN72] J. Janov *et al., J. Nucl. Mater*., 1972, vol. 44, p.61.
[KAH22] O. Kahraman *et al., J. App. Phys., 2022, vol.* 132, p. 115106.
[KAT08] M. Kato *et al*., *J. Nucl. Mater., 2018, vol.* 373, p. 237- 245.
[KAT16] U. R. Kattner, *Tecnologia em Metalurgia Materiais e Mineração* ,2016, vol *13*, chap. 1, p 3-15.
[KUT00] T. R. G. Kutty *et al*., *J. Nucl. Mater.,* 2000, vol. 282, p.54-65.
[LAI19] M. Lainet *et al*., *J. Nucl. Mater*., 2019, vol. 516, p. 30-53.
[LEI15] G. Leinders *et al*., *J. Nucl. Mater.*, 2015, vol. 459, p. 135–142.
[LI16] H. Li *et al.*, J. Alloys Compd., 2016, vol. 682, p.132.
[LIV06] T. Livneh *et al.*, Phys. Rev. B, 2006, vol. 73, p. 1.
[LIV22] T. Livneh, Phys. Rev. B, vol. 105, p. 45115.
[MAN12] S. Manna *et al*., *J. Nucl. Mater*., 2012, vol. 424, p. 94.
[MAN12-2] S. Manna *et al*., *J. Nucl. Mater*., 2012, vol. 426, p. 229.
[MAR17] P. M. Martin *et al.*, « ESNII+ : Catalog on MOX properties for fast reactors »,FR17, 2017.
[MAR66] P. Marlow *et al*., *Philosophical Magazine*., 1966, vol. 14, p. 409.
[MAS17] A. Maslova *et al.* , Mater. Charact., 2017, vol. 129, p.260.
[MED20] L. Medyk *et al*., *J. Nucl. Mat. ,2020, vol.* 541, p. 152439.
[MEN69] M.I. Mendleson, *J. Am. Ceram*. Soc., 1969, vol 52, p. 443-446.
[MUR01] B.N. Murty *et al., Powder Technol.,* 2001, vol. 115, p.167.
[NAJ17] M. Naji *et al*., *Phys. Rev. B*., 2017, vol. 95, p. 104307.
[NJI20] I. Cheik Njifon, E. Torres, J. of Nucl. Mater., 2020, vol. 537, p. 152158.
[PEL20] M. Pelletier and Y. Guérin, *Comp. Nucl. Mater*., 2020, vol. 2, p. 72-105.
[PAW81] G. S. Pawley, *J. Appl. Cryst.,* 1981, vol. 14, p. 357-361.
[QUE18] A. Quemet *et al*., *J. of Mass Spectrom.*, 2018, vol. 431, p. 8-14.
[QUE19] A. Quemet *et al*., *J. of Rad. And Nucl. Chem.*, 2019, vol. 321, p. 997-1004.
[SAR70] C. Sari *et al*., *J. Nuc. Mat*, 35, 1970, p. 267-277.
[SARS12] M.J. Sarsfield *et al*., J*. Nucl. Mater*., 2012, vol. 427, p.333–342.
[SCH12] J. Schindelin et al., *Nature Methods*, 2012, vol. 9, p. 676- 682.
[SIM22T] J. Simeon, thesis, Frittage et développement de la microstructure du combustible nucléaire MOX RNR, Université Grenoble Alpes, 2022.
[STA17] D. Staicu *et al.*, « New catalog on $(U,Pu)O_2$ properties for fast reactors and first measurements on irradiated and non-irradiated fuels within the ESNII+project. » European Commission, 2017.
[STR16] M. Strach *et al., Nucl. Instrum. Methods Phys. Res*. B, 2016, vol. 374, p. 125-128.
[SUN85] B. Sundman *et al*., *Calphad*, 1985, vol. 9, chap. 2, p.153–190.
[TAK20] C. Takoukam-Takoundjou *et al.*, *J. of Nucl. Mater*., 2020, vol. 534, p. 152125
[TAL15] Z. Talip *et al*., J. *Am. Ceram. Soc.*, 2015, vol. 98, p. 2278–2285.
[TAL17] Z. Talip, et al., J. Raman Spectrosc., 2017, vol. 48, p. 765.
[TAL18] Z. Talip *et al*., J. Nucl. Mater., 2018, vol. 499, p. 88.
[TRE06] H. R. Trellue, Progr. In Nucl. Ener., 2006, vol. 48, p. 135-145

[TRU13T] T. Truphemus, thesis, Etude des équilibres de phases en fonction de la température dans le système UO_2PuO_2-Pu_2O_3 pour les céramiques nucléaires aux fortes teneurs en plutonium., Aix-Marseille Université, 2013.
[TRU13] T. Truphémus et al., *J. Nucl. Mater.,* 2013, vol. 432, p. 378-387.
[VAU14T] R. Vauchy, thesis, Etude du rapport O/M dans des combustibles oxydes à base d'U et Pu : élaboration et caractérisation de matériaux modèles $U_{1-y}Pu_yO_{2-x}$, Université de Grenoble, 2014.
[VAU14] R. Vauchy *et al., Ceram. Int.,* 2014, vol. 40, p. 10991-10999.
[VAU15] R. Vauchy *et al., J. Nucl. Mater.,* 2015, vol. 465, p. 349-357.
[VAU21] R. Vauchy *et al*., *J. Appl. Cryst*., 2021, vol. 54, p. 636-643.
[VIL19] Villa-Aleman *et al*., *J. Nucl. Mater*., 2019, vol. 515, p. 140–149.
[VIL21] E. Villa-Aleman *et al*., *J. Raman Spectrosc.*, 2021, vol. 52, p.1486-1489.